Simulation Standard

Engineered Excellence

A Journal for Process and Device Engineers

Modeling the Optical Response of Phonon-dressed Excitons in OLED Simulations

Abstract

We demonstrate the modeling of optical response of exciton-polarons based on the well established Holstein Hamiltonian to model coupled exciton-phonon systems in organic molecular chains. Our approach uses Green's functions to compute the density of states and the linear optical susceptibility, and thus eliminates the conventional and computationally expensive step of diagonalizing a large Hamiltonian matrix. We exploit this technique further to focus exclusively on the optically active states when computing the linear optical response, and significantly reduce the computational effort to construct the optical susceptibility. In this article, we demonstrate the computation of absorption and emission spectra of Alq_3 at 4.2 K and at room temperature using our model. Using the two parameters of the Holstein model, the inhomogeneous broadening energies, and a phenomenological reorganization energy of the solute, we obtain excellent fits to established experimental results. We then use this model inside the larger simulation of a 3-layer organic light emitting (OLED) structure composed of Alq_3, Alq_3:DCJTB, and α-NPD, which are the electron transport, emissive, and hole transport layers respectively. In our methodology, we also couple the optical response into the rate equations for exciton dynamics in addition to computing the spectrum of light output by the device.

Keywords: Frenkel Exciton, Phonon, Organic, OLED, tris-hydroxyquinoline, Holstein model, Optical emission, Optical absorption

I Introduction

Organic light emitting (OLED) and photovoltaic (PV) technologies are growing at a rapid pace. Compared to the inorganic semiconductor based technology, organics provide much simpler and cheaper fabrication methodologies. With continuing research in this field, a vast number of organic materials have become potential candidates for device applications, and they generally exist in diverse forms ranging from crystalline phases to fully disordered solutions. This provides a challenge for developing reliable and widely applicable models for understanding experimental data and predicting device characteristics.

Yet the optical and transport properties of these materials can often be captured via models with one or more excited states (excitons) hopping on the underlying molecular lattice, and linearly coupled to its internal vibrational modes[1–3]. Each type of vibrational mode can in turn be modeled as a harmonic oscillator. Here we describe a methodology that exploits this fact to simulate exciton dynamics and light emission from OLEDs. The primary purpose of this work is to provide a physically based model to compute the optical response with a small set of parameters.

Materials for which a widely accepted measured spectrum over the desired energies does not exist are a clear target application. The model is also relevant for well known materials since the optical response for most organic systems varies widely due to their sensitivity to their environments and their contact with charge injection layers in devices. With a small parameter set in which parameters are related to fundamental physical mechanisms, the present model calibrated against experimental data acquires predictive value for exploring an entire class of devices. For instance emissive layers with similar vibrational modes, excitonphonon coupling, and inhomogeneous broadening can fall within the range of a single model fit once to reliable experimental data.

Continued on page 2 ...

INSIDE

Atlas Simulation of GaN-Based Super Heterojunction Field Effect Transistors Using the Polarization Junction Concept 9

Hints, Tips and Solutions 11

Our methodology applies to electroluminescent organic materials such as Alq_3, DCM, DCJTB etc., which are generally a mixture of short chains of molecules, or independent units with random orientations for the dipolar charge excitations[2, 4, 5]. Electrons and holes injected into these materials form *Frenkel excitons*, in which both the electron and the hole reside on the same molecular unit. For example in Alq3, the exciton forms by electron transition from phenoxide to the the pyridyl ring of a single molecule[6, 7].

Radiative recombination of excitons gives rise to luminescence. In the absence of spin-orbit coupling (SOC), photons are emitted only by singlets due to the optical selection rules. Heavy metal impurities are increasingly being used to enhance radiative annihilation of triplets with SOC[4, 8, 9]. One of the main attractions of using organic materials is that the color of emitted light can be easily controlled by doping with molecules of different band gaps[4]; the relative population of excitons on each species determines the overall shift in the main emission wavelengths. The transfer of excitons between the host and the dopant controls the relative populations, and this transfer is fundamentally driven by Förster energy transfer[2, 10–13] for singlets and Dexter transfer[2, 14, 15] for triplets. In our methodology, the radiative and transfer rates are computed from the quantum mechanical model for the optical response of each species.

One of the most important aspects of Frenkel excitons in organic materials is their strong modification by the internal vibrational modes of the molecular units[1–3, 16–20]. These modes may vary from bending, stretching, or rotational modes, and they can range from being localized at one molecule to being spread out over an entire polymer chain. Providing great simplification in modeling is the unifying aspect of these modes: their energies tend to be insensitive to the presence of an exciton, and their coupling to the excitons is linear[26]. The magnitude of the linear coupling gives a timescale for i*ntra-molecular relaxation*. The localized vibrational mode follows the exciton if the intra-molecular relaxation is faster than inter-molecular charge transfer[3]. This effectively *dresses* the exciton with a phonon cloud, creating a new quasi-particle, called an *exciton-polaron*, which has different transport and optical properties than the bare electron-hole pair comprising the Frenkel exciton. In our methodology, we compute the optical properties for this composite quasi-particle, thus taking into account the strong phonon dressing exactly within the model of linear coupling.

Figure 1 summarizes the radiative transitions between vibrational modes of typical organic molecules. The vibrational energy of the molecule defines a potential energy surface, which can be approximated as a parabola (in nuclear coordinates) near equilibrium. If no coupling to phonons existed in the molecule, the emission and absorption spectra will both consist of a single peak represented by the green line in Figure 1. called the *zero-phonon* transition, which is between 0 and 1 exciton states containing no phonons. In the presence of coupling to phonons, optical excitation creates both the exciton and its phonon cloud. The blue line indicates transitions from the lowest vibrational state (the only state at 0 K) to 1-exciton state containing one or more phonons. These transitions give a progression of uniformly spaced peaks above the zero-phonon transition, which merge into a single broad spectrum after inhomogeneous broadening is taken into account.

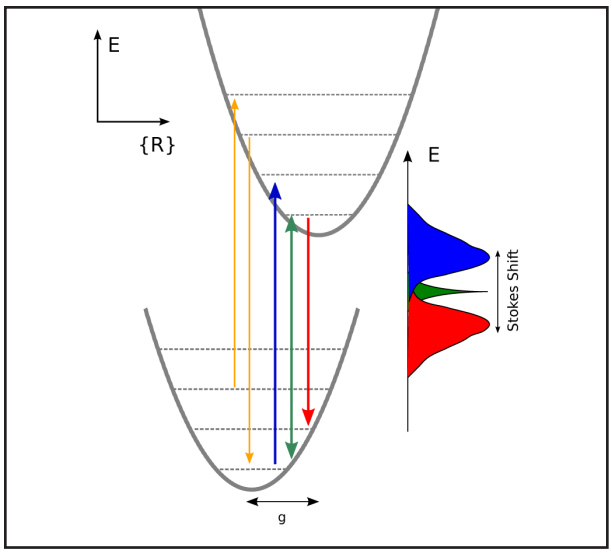

Figure 1. Schematic illustration of the fundamental optically driven transitions in the presence of exciton-phonon coupling. The vertical scale is energy, and the horizontal scale is a set of generalized nuclear coordinates. The lower parabola represents the potential energy surface of the electronic ground state (0 exciton), and the upper parabola represents the potential energy surface of the first excited state (containing 1 exciton). The dashed horizontal lines indicate the quantized energy levels of the vibrational potential (phonons). Both energy surfaces are modeled using the same parabolic potential, and thus the modes in each are those of a harmonic oscillator. The wavefunctions in the upper level are shifted by amount *g* that parameterizes the exciton-phonon coupling. The peaks on the right schematically depict the emission (red), absorption (blue) and zero-phonon line (green).

In the emission spectrum, the phonon occupation of the ground state is probed. The red line indicates luminescence transition in which the exciton, having achieved quasi-equilibrium to its lowest energy state, recombines and leaves the molecule in a vibrational state with one or more phonons. These transitions give peaks in emission spectra progressing below the zero-phonon line. Finally, the two yellow lines indicate excitations that occur due to thermal excitations of phonons in the ground state, and the excited state at quasi-equilibrium. These transitions are suppressed exponentially by the corresponding Boltzmann factors.

As explained in the next section, the zero-phonon transition is almost invisible in most systems because the overlap of nuclear wavefunctions in the 0 and 1-exciton manifolds is much higher at intermediate phonon occupations. This results in a difference in the location of peaks in the absorption and emission spectra, known as the *Stokes shift*. The Stokes shift in organics is driven both by the above mentioned overlap, and by the *reorganization energy* of the environment when an exciton is introduced into it[7, 21–23]. The former is calculated in our model from the exciton phonon coupling, and the latter is used as a parameter since it is impossible to calculate reorganization energy of an arbitrary environment.

In Section II, we provide the theoretical background and discuss the salient aspects of computation of spectra in our approach. In Section III, we discuss results of our computations for Alq_3 and compare them with experimental data. We then discuss simulation of a 3-layer OLED device based on Alq_3 : DCJTB. Finally we conclude in Section IV.

II Methodology

A. Structure and Setup

At the top level of the simulation in Atlas, we solve the coupled rate equations for densities of electrons, holes, intrinsic excitons and dopant excitons (see Section 15.3 of Atlas manual). Ignoring the Stark effect[21], the energy levels of the molecules do not shift with bias and therefore we compute the optical response for unit density of both the intrinsic and dopant molecules separately at the beginning of the simulation. At subsequent bias steps, this spectrum is used to compute radiative loss of excitons and coupling between the intrinsic and dopant singlets fully self-consistently with the quantum mechanical model of fluorescence. The total fluorescence from each mesh node is computed by combining the spectra the exciton density on each node. When used in conjunction with ray tracing, transfer matrix, or finite difference time domain algorithms, the total fluorescence spectrum gives the angular and spectral characteristics of the light output by the device [27].

The simulation is setup by dividing a device into regions, and associating a material with each region. We have extended the `MATERIAL` statement in Atlas to facilitate the addition of up to 10 different exciton species per region. An exciton-polaron species is added by specifying the parameter `ADDPOLARON` and specifying a name for the species as `MIX.NAME=name`. At present the rate equations are limited to two species per node only. Specifying the `HOLSTEIN` parameter for a particular region initiates the quantum calculation of optical response for each species defined in the region. Since the model described below does not depend explicitly on the spatial distribution of excitons, a single model per species is solved for each region, rather than each mesh node. This simplification is correct as long as spatial distribution of energy levels can be captured by inhomogeneous broadening. When this cannot be justified, it is best to divide up a region into smaller pieces over which we expect energy levels and their couplings to lie within inhomogeneous broadening.

Below we describe the Hamiltonian for quantum mechanical description of exciton-polaron dynamics in an organic materials. We then describe our computation of optical response and the main physical quantities calculated in the simulation.

B. Exciton-polaron states

The fundamental description we use here for the exciton-phonon system is given by the Holstein Hamiltonian,

$$H = J\sum_n \left(a_n^\dagger a_{n+1} + a_{n+1}^\dagger a_n\right) + \sum_n a_n^\dagger a_n \left[-g(b_n^\dagger + b_n) + g^2 + E_0\right] + E_{vib}\sum_n b_n^\dagger b_n, \quad (1)$$

where a_n, $a_n^\dagger$ annihilate and create an exciton at molecular site n respectively, while b_n and $b_n^\dagger$ perform the same function for phonons. The parameter J is the hopping energy, g is the exciton-phonon coupling, E_0 is the band gap or the difference between the HOMO and the LUMO levels (see Figure 1), and E_{vib} is the energy of a single excitation (phonon) of the vibrational mode. The term proportional to g^2 (1) aligns the LUMO level and the band gap to the user specified value. The band gap E_0 plays no essential role in determining the eigenvalues and eigenstates of the system, except for shifting the resulting spectrum by the band gap energy. Note that the above form of the Hamiltonian does not make reference to the detailed spatial structure of the exciton and nuclear wavefunction. That information has been absorbed into the parameters described above.

Following Hoffman *et. al.* [3] we compute the energy spectrum of this Hamiltonian in the basis represented as $|n\rangle\,|\underline{\nu}_n\rangle$, where $|n\rangle$ represents exciton at site n, and $|\underline{\nu}_n\rangle = |\ldots \nu_{n-1}, \tilde{\nu}_n, \nu_{n+1}, \ldots\rangle$ represents a *phonon cloud* with ν_m specifying the phonon occupation in the oscillator at site m. The oscillator at the exciton site is shifted by amount g (Figure 1) as dictated by (1), and we represent its occupation number by a different symbol $\tilde{\nu}$.

Thus by virtue of the dependence of phonon occupation on the location of exciton, the state of the molecular distortion is coupled fully to the exciton. The resulting Hamiltonian can be diagonalized using the Lang-Firsov transformation[3], in which the system is described by exciton-polaron whose hopping energy is given by $J \times F_n^{\pm}$, where where $F_n^{\pm}$ are called *Frank-Condon* factors, and they are equal to the overlap of the phonon clouds at the initial and final site in a hopping event.

The main benefit of using harmonic oscillator to model the vibrational modes is that Frank- Condon factors can be computed analytically from the inner product of shifted oscillator wavefunctions. Thus the two parameters, J and g, fully determine the effective mass of the polaron. The same Frank-Condon factors also determine the amplitudes and selection rules of optical transitions.

A fully cohrent exciton-polaron in a lattice carries a definite momentum, and the energymomentum relationship yields a set of exciton bands as a function of the momentum k. Since the photon momentum is negligible compared to that of an exciton, optically driven transitions occur only at $k = 0$. We therefore compute only $k = 0$ states and exploit the fact that large inhomogeneous broadening rather than band dispersion dominates density of states at $k = 0$. This formulation of the DOS is also consistent with assumptions underlying the hopping model of exciton dynamics simulated in Atlas.

C. Radiative Emission and Energy transfer

Following the standard treatment of dipole coupling between light and matter, the Hamiltonian for the interaction of an exciton-polaron with a plane wave electric field is,

$$H_{op}(t) = -e\sum_{\alpha}\mathbf{E}_{\alpha}e^{-i\omega_{\alpha}t}\hat{\mathbf{d}},$$

where the sum includes both positive and negative frequencies, and $\hat{\mathbf{d}}$ is the position operator.

A standard approach to compute absorption and emission spectra is in terms of the matrix elements of $\hat{\mathbf{d}}$ taken between the exact eigenstates of exciton-polarons. This is an extremely expensive calculation since a very large number of phonon cloud states exist for a given modest size and phonon occupancy. In addition, since most of the states are optically forbidden, their inclusion in the spectrum serves only as an additional broadening mechanism.

In our methodology, we use a much faster Green function based method to compute the absorptive and emissive contributions optical susceptibility: $\chi_{ab}(\omega)$, $\chi_{em}(\omega)$ respectively. In this method, only the optically accessible states are referenced explicitly by the calculation, while the presence of the remaining states appears as an additional broadening mechanism as is expected physically. The technique is mathematically equivalent to exact diagonalization, and becomes useful in the presence of sufficient broadening as is the case for organic materials[28].

With homogeneous broadening, specified by η, the susceptibility can be written as,

$$\chi_{ab}(E) = -\frac{e^2\varrho}{\epsilon_0}\sum_{\nu}\langle 0,\nu|\,\hat{d}\,[E-H-i\eta]^{-1}\,\hat{d}\,|0,\nu\rangle\,\frac{e^{-\nu E_{vib}/k_BT}}{Z}, \quad (2)$$

$$\chi_{em}(E) = -\frac{e^2\varrho}{\epsilon_0}\sum_{\alpha}\langle 1,\alpha|\,\hat{d}\,[E-H-i\eta]^{-1}\,\hat{d}\,|1,\alpha\rangle\,\frac{e^{-N(\alpha)E_{vib}/k_BT}}{Z}. \quad (3)$$

where ϱ is the density of molecules, and N(α) is the number of phonons in the exciton-polaron state Ψ_{α}, and Z is the partition function normalizing the Boltzmann factors. Computation of $\chi_{abs}(\omega)$, $\chi_{em}(\omega)$ by (2) and (3) is done by solving a series of linear systems. By organizing the basis states according to whether they are dipole allowed or not, we minimize the number of systems that must be solved. The spectra are subjected to energy-dependent inhomogeneous broadening in the end.

The power radiated per unit volume in energy interval $[E,\ E + \Delta E]$ by spontaneous emission is given by the imaginary component of χ_{em},

$$W_{sp} = \frac{f_{orient}}{\hbar}\int_{E}^{E+\Delta E}dE'\frac{E'^4}{\pi^2(\hbar c)^3}\chi_{I;em}(E'), \quad (4)$$

where f_{orient} accounts for averaging over the random orientations of the exciton dipoles in amorphous materials. Thus the radiative rate, normalized to 1 exciton per unit cell volume is,

$$k_{rad} = \frac{1}{\hbar}\frac{\Omega}{3\pi^2\,(\hbar c)^3}\int_0^{\infty}dE\,E^3\chi_{I;em}(E). \quad (5)$$

In the case of doped materials, the Förster transfer rate of a singlet from donor site D to acceptor A is,

$$k_{dd} = \frac{\kappa^2}{8\pi^3R^6\hbar}\int dE\Omega\chi^{A}_{I:abs}(E)\Omega\chi^{D}_{I:em}(-E). \quad (6)$$

From this formula we also compute the F¨orster radius, which is inter-molecular distance at which the non-radiative transfer equals the radiative decay of excitons. Note that conventional formulas for Forster transfer use slightly different definitions for the spectra used in the overlap integral (6). See Appendix A for equivalence of k_{dd} to conventional formula.

We now turn to results of our simulations with this model.

III Results and Discussion

A. Spectrum of Alq_3

Alq_3 is one of the most important host materials used in OLEDs. It is known to emit green light at wavelengths of approximately 530 nm. In addition, it is also one of the simplest applications of the model described above. Frenkel excitons in Alq_3 couple to the bending modes of the molecule where the exciton resides. However the inter-molecular hopping is weak, and thus the vibrational modes of Alq_3 are expected to create small phonon clouds only. The large inhomogeneous broadening generally render the vibrational modes unobservable in the emission and absorption spectra of Alq_3.

However, in their experiments, Brinkman *et. al.* were able to obtain this for crystalline Alq_3 at 4.2 K [23]. From their observations, the authors concluded that the Huang-Rhys factor, $(g/E_{vib})^2 \approx 2.6 \pm 0.4$, and $E_{vib} = 0.065$[22, 23]. Using the value $g = 1.6E_{vib}$ in our model, and setting the

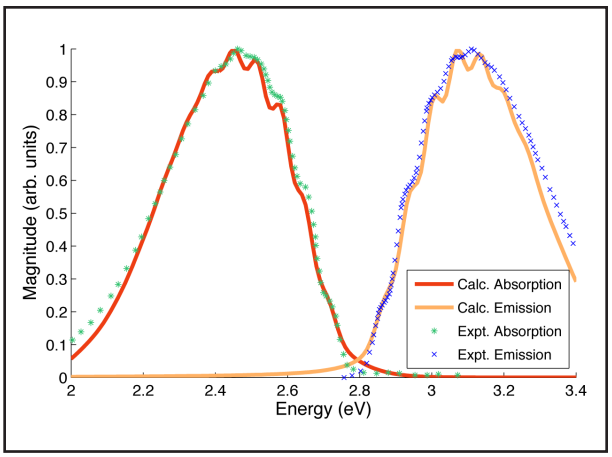

Figure 2. Comparison of the calculated Alq3 spectra to those measured at for the crystalline phase at 4.2 K. The dots and crosses are digitized experimental data from [23]. Homogeneous broadening was set to 10 meV and inhomogeneous broadening to 22 meV. A single Voigt lineshape is added for both the emission and absorption to take into account the background dielectric due to higher energy states.

hopping parameter $J = 0.1E_{vib}$, we computed spectra for a single Alq_3 region using our model inside Atlas. We varied the phonon cloud sizes from 1 (on-site vibron) to 4 and noticed only small changes in the spectra, which is expected due to the fact that g suppresses hopping exponentially. As was discussed in Section I, two additional parameters are needed: a band gap and a Stokes shift. Here we used a band gap of 2.87 eV, and an additional Stokes shift of 0.15 eV. These parameters alone correctly reproduce the absorption spectrum below the peak and emission spectrum above the peak, in particular the vibronic structure (peaks along the spectral backbone), as shown in Figure(2).

However high energy modes and the background dielectric add additional featureless profile to the measured spectrum. These are often modeled as highly broadened extra energy levels. We model these as Voigt lineshapes (Gaussian convolved with Lorentzian) by using the parameter `ADDSTATE` on `MATERIALS` statement of the corresponding region. The lineshape center is specified using `EX.ECEN` or `GS.ECEN` depending on whether the state is added to the 1-exciton or 0-exciton states respectively. The parameters `EX.HOMOBROADENING` and `EX.INHOMOBROADENING` must be used to specify the corresponding values of broadening in electron volts. The extra lineshapes in the present calculation are centered at 3.2 and 2.4 eV, with both the homogeneous and inhomogeneous broadening both set to 10 meV.

We now consider room temperature spectrum at 300 K, the emission spectrum of a thin Alq_3 film exhibits no vibronic structure and is left as a smooth profile, shown in Figure 3. In this calculation, we used larger inhomogeneous broadening of 150 meV, and did not use extra Voigt lineshapes to account for the background dielectric. Thus a combination of 2-parameter Holstein model, and a broad extra energy level can be used to successfully reproduce experimental spectra for this material. We remark that the size and the occupancy of the phonon clouds are not free parameters, as both these should be increased until the results converge.

B. Light emission from Alq3:DCJTB based OLED

We now demonstrate the ability to apply this model in simulating a typical 3-layer OLED. The left panel in Figure 4 shows the structure of the device simulated. The device is composed of a 30 nm wide emission layer (EML) with the host Alq3 doped to 1% with DCJTB. At the top of EML is a 30 nm thick electron transport layer (ETL) of pure Alq3, and at the bottom is a hole transport layer (HTL) with material properties corresponding the α-NPD. The main energy level requirements to make this device emit are as follows. The LUMO levels of the ETL and EML are aligned to facilitate electron injection into the EML, while that of the HTL is about 300 meV higher. Thus HTL essentially acts as an electron blocking layer and maximizes recombination of electrons with holes in the EML. Similarly, the HOMO level of the HTL is only slightly above the HOMO level of the EML, which facilitates hole injection, while the HOMO level of ETL is much lower to block holes at the EML/HTL interface.

We used the organic defect model described in *Atlas User's Manual* to simulate exciton transport in each layer. The Holstein model was applied to ETL and EML for computing the emission spectra and the radiative as well as Förster rates. We used the Poole-Frenkel field-dependent mobility model, with parameters taken from [24]. The right panel in Figure 4 shows the typical current-voltage relationship of an LED.

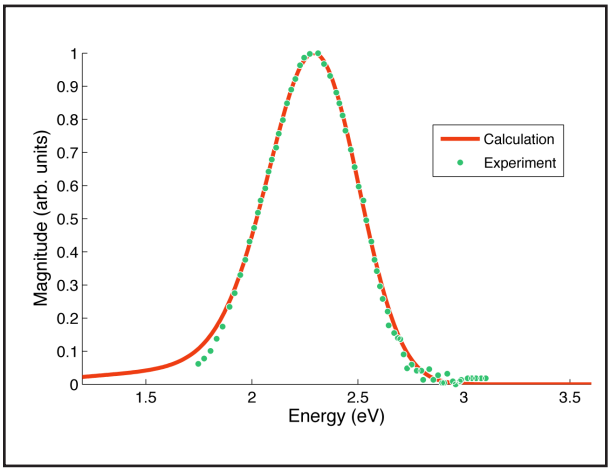

Figure 3. Comparison of the calculated Alq3 absorption spectrum to the measured spectrum for a thin film at 300 K. The dots and crosses are digitized experimental data from [23]. A single Voigt lineshape is added to take into account the background dielectric due to higher energy states.

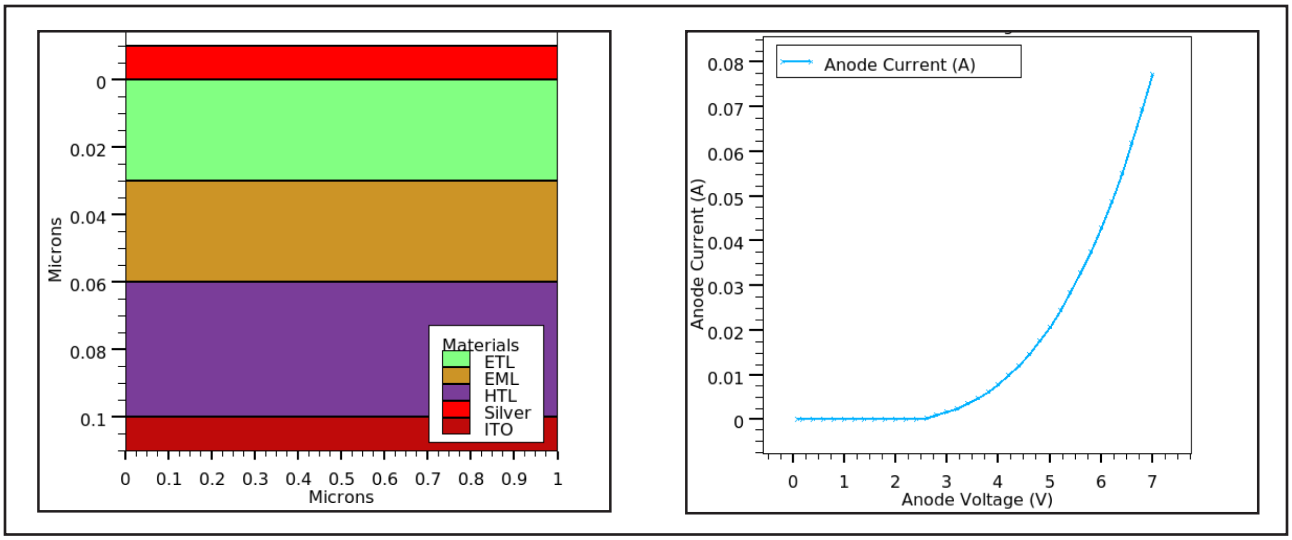

Figure 4. Left: Structure of the three layer device with 30 nm electron transport layer with Alq3, 30 nm emission layer with Alq_3:DCJTB and a 40 nm hole transport layer of α-NPD. Right: Current-Voltage characteristics of 3-layer device, intrinsic and dopant exciton densities, Langevin recombination rates, and the Forster exchange per unit volume.

In Figure 5 we show the density of host and dopant excitons in the ETL and EML layers. Good injection of carriers into the active region (EML) is apparent from the much larger magnitude of the densities in the EML. For a given Förster radius following from the device spectrum, the relative fraction of dopant excitons to host excitons is highly sensitive to the ratio of this radius to host-dopant distance. We set the inter-molecular distance equal to 3.7 nm in these simulations, corresponding to host density of approximately 4×10^{18} cm^{-3}. The simulation yields a Förster radius to be approximately 3.6 nm for exciton transfer to the dopant. The radius is approximately 1 nm for the reverse process. Thus exciton migration to the dopant is very nearly one directional.

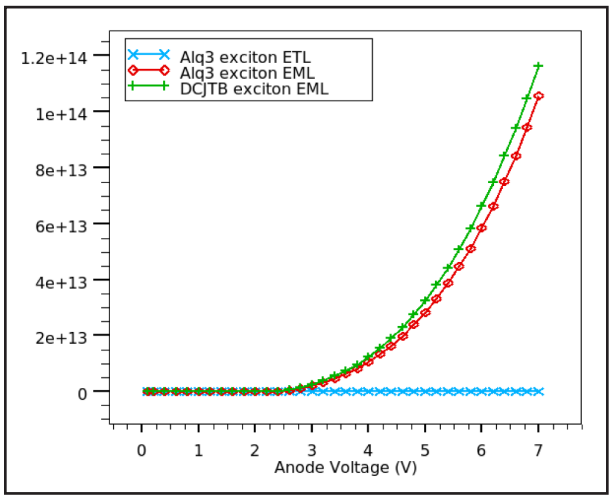

Figure 5. Densities of excitons (cm^{-3}) on Alq_3 and DCJTB in the electron transport and emissive layers (left). Spectrum of light emitted from the EML layer (right) and computed using reverse ray trace with source terms restricted to the respective layers. The larger density of excitons on DCJTB explains the overall shift in the spectrum from the host to dopant emission wavelength.

Figure 6. shows the average number of radiative transitions, Förster transfers and Langevin recombinations per unit volume per time. The Förster rate exceeds radiative rates for each species, and thus we expect the dopant to make significant contribution to the output spectrum of light. The large Förster rate is due to a good overlap between the absorption spectrum of the dopant and emission spectrum of the host, as displayed in the left panel of Figure 7.

At the final bias point of 7 V, we performed a reverse ray trace analysis to compute the light output by the device. The resulting spectrum is shown in the right panel of Figure 7. The output spectrum is clearly dominated by emission from the dopant, while the emission from the host contributes the smaller peak on the higher energy side. Thus the effect of Forster transfer on the emission spectrum is captured quite well by the simulation.

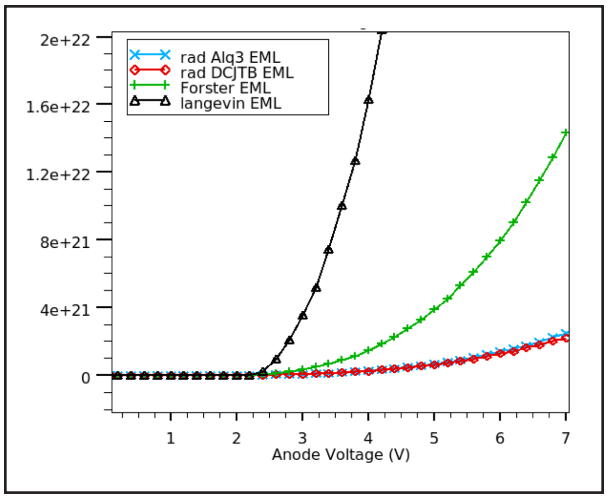

Figure 6. The radiative emission rates, Forster transfer rates and Langevin recombination rates per unit volume as a function of bias voltage. Vertical scale: $1/(cm^3$ &).

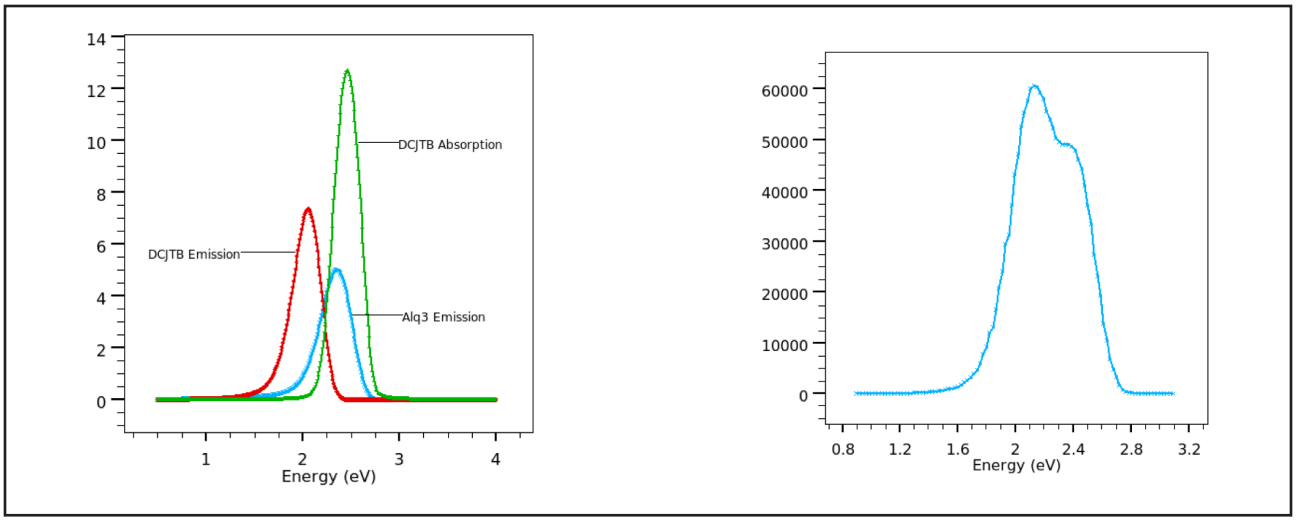

Figure 7. Emission and absorption spectra for the host (Alq_3) and the dopant DCJTB. The good overlap between host emission and dopant absorption yields high F¨orster transfer rates. The vertical scale on the left panel indicates the response from a volume of 1 molecular unit. The vertical scale on the right panel is the power spectral density.

IV Conclusion

We have implemented the calculation of OLED optical response using the Holstein Hamiltonian. The shape of spectra is determined by only 2 parameters while the additional parameters account for the position and scaling. The computation is fully integrated with the LED device simulation in Atlas. This integration is performed both at the level of light output coupling as well as at the deeper level of determining the radiative and excitation transfer rates in exciton dynamics. With the addition of Voigt lineshapes to model the background dielectric contributions, we have demonstrated the model to fully capture the important physical features of measured spectra for Alq_3. We demonstrated the full methodology of using this model in Atlas by simulating a typical 3-layer OLED device with a doped emissive layer. We extracted the dynamical rates computed using our model within each region, and verified that the relative magnitudes of the dynamical rates are well correlated with the main qualitative aspects of the emission and absorption spectra of the host and dopant molecules.

References

[1] M Hoffmann, Z G Soos, K Leo. Absorption Spectra [1] M. Hoffmann, Z. G. Soos, and K. Leo, 237 (2006)

[2] V. Agranovich, Excitations in Organic Solids (Oxford, 2009)

[3] M. Hoffmann and Z. Soos, Phys. Rev. B 66, 024305 (2002)

[4] S. Reineke, M. Thomschke, B. L¨ssem, and K. Leo, Rev. Mod. Phys. 85, 1245 (2013)

[5] L. Hung and C. Chen, Mater. Sci. Eng. R Reports 39, 143 (2002)

[6] M. D. Halls and H. B. Schlegel, Chem. Mater. 13, 2632 (2001)

[7] O. Gardens, ed., Trends in Optical Materials (Nova, 2007)

[8] H. Kanno, N. C. Giebink, Y. Sun, and S. R. Forrest, Appl. Phys. Lett. 89, 023503 (2006)

[9] Y. Sun, N. C. Giebink, H. Kanno, B. Ma, M. E. Thompson, and S. R. Forrest, Nature 440, 908 (2006)

[10] T. Forster, Discuss. Faraday Soc. 27, 7 (1959)

[11] D. Beljonne, C. Curutchet, G. D. Scholes, and R. J. Silbey, 113 (2009)

[12] G. D. Scholes, Annu. Rev. Phys. Chem. 54, 57 (2003)

[13] G. Scholes and D. Andrews, Phys. Rev. B 72, 125331 (2005)

[14] A. K¨hler and H. B¨ssler, Mater. Sci. Eng. R Reports 66, 71 (2009)

[15] A. Olaya-Castro and G. D. Scholes, Int. Rev. Phys. Chem. 30, 49 (2011)

[16] I. Vragovi´, R. Scholz, and M. Schreiber, Europhys. Lett. 57, 288 (2002)

[17] I. Vragovi´ and R. Scholz, Phys. Rev. B 68, 155202 (2003)

[18] J. T. Devreese and A. S. Alexandrov, Reports Prog. Phys. 72, 066501 (2009)

[19] N. Karl, Synth. Met. 133-134, 649 (2003)

[20] Y. Zhao, G. Li, J. Sun, and W. Wang, J. Chem. Phys. 129, 124114 (2008)

[21] R. Boyd, Nonlinear Optics (Academic Press, 2003)

[22] M. Muccini, M. Brinkmann, G. Gadret, C. Taliani, N. Masciocchi, and A. Sironi, Synth. Met., 122, 31 (2001)

[23] M. Brinkmann, G. Gadret, M. Muccini, and C. Taliani, J. Am. Chem. Soc. 122, 5147 (2000)

[24] C.-C. Lee, M.-Y. Chang, P.-T. Huang, Y. C. Chen, Y. Chang, and S.-W. Liu, Journal of Applied Physics 101, 114501 (2007)

[25] V. G. Kozlov, V. Bulovic, P. E. Burrows, M. Baldo, V. B. Khalfin, G. Parthasarathy, S. R. Forrest, Y. You, and M. E. Thompson, J. Appl. Phys. 84, 4096 (1998)

[26] From experimental data, linearity is implied by the presence of uniformly spaced peaks in both photoluminescence (PL) and photoluminescence excitation (PLE) spectra. The insensitivity to excitation follows from the spacing being the same in both PL and PLE spectra.

[27] This creates a feedback mechanism whereby one can create a strongly non-linear dependence of the emission spectrum on bias. However, this is not generally seen in common materials

and thus within the most common parameter regime of the model explored here.

[28] The technique requires too many Green function evaluations to be useful when broadening is negligible.

Appendix A: Derivation of conventional formula for Förster radius

Absorption cross section $\sigma = \alpha V/N = \Omega\chi_{I;abs}(\omega)\omega/c$, as there is 1 molecule in volume Ω. Take the ratio to radiative, while substituting absorption cross section and fluorescence spectrum,

$$\frac{k_{NR}}{k_{rad}} = \frac{3\kappa^2 c^4}{8\pi r^6}\frac{\int d\omega \sigma^A(\omega)F^D(\omega)\omega^{-4}}{\int d\omega F^D(\omega)}.$$

If we normalize F^D such that $\int d\omega\ \hat{F}^D(\omega) = 1$, or $\hat{F}(\omega) = F(\omega)/(\hbar k_{rad})$. We now get the traditional formula[10, 25]

$$k_{NR} = k_{rad}\frac{1}{r^6}\left[\frac{3\kappa^2}{8\pi}\int d\omega \frac{c^4}{\omega^4}\sigma^A(\omega)\hat{F}^D(\omega)\right] = k_{rad}\left(\frac{R_0}{r}\right)^6.$$

Atlas Simulation of GaN-Based Super Heterojunction Field Effect Transistors Using the Polarization Junction Concept

Introduction

Wide-bandgap semiconductors such as SiC and GaN have attracted much attention because they are expected to break through the material limits of silicon. In particular, AlGaN/GaN HEMTs are generally promising candidates for switching power transistors due to their high electric field strength and the high current density in the transistor channel giving a low on-state resistance.

Field plate (FP) technologies are generally used in order to manage surface electric field distribution of GaN HEMTs. Recently, GaN Super Heterojunction Field Effect Transistors (Super HFETs) based on the polarization junction (PJ) concept have been demonstrated [1, 2]. This concept is based on the compensation of positive and negative polarization charges at heterointerfaces such as AlGaN/GaN to achieve similar effect to RESURF or Super Junction (SJ) in silicon devices.

In this article, we will demonstrate the Atlas device simulation of GaN Super HFETs in comparison with the experimental data based on [1, 2]. Convergence difficulties in this simulation generally arise from the formation of large polarization charges and the use of abrupt heterojunctions with a Schottky gate, as well as the existence of a p-GaN base region and a floating undoped-GaN region. Atlas's sophisticated physical models properly account for all physical mechanisms inherent in a GaN Super HFET structure, thereby ensuring well-converged solutions with consistent simulation results.

Device Structure and Physical Models

The Super HFET structure created by Atlas syntax is shown in Figure 1. The layer structure consists of an undoped double-hetero GaN/AlGaN/GaN structure with a p-GaN cap layer. The feature of the Super HFET structure is the presence of the 2-D hole gas (2DHG) induced by negative polarization charge at the upper GaN/AlGaN heterointerface as well as the 2-D electron gas (2DEG) at the lower AlGaN/GaN heterointerface. The computation of 2DEG and 2DHG due to polarization effect was performed automatically during the simulation with our built-in model [3]. The Super HFET has four electrodes: source, gate, base, and drain. The source and drain electrodes form ohmic contacts to the 2DEG by setting their work function identical to the electron affinity of the AlGaN layer. The gate forms a Schottky contact to the AlGaN layer. The base electrode makes an ohmic contact to the 2DHG through the top p-GaN layer and is electrically connected to the gate by specifying COMMON parameter on the CONTACT statement.

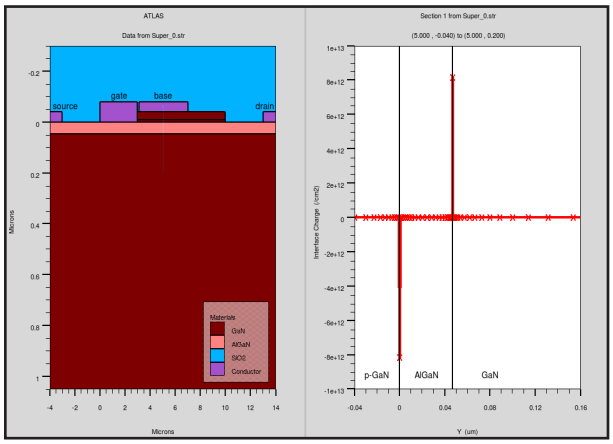

Figure 1. Cross sectional diagram of a GaN Super HFET (left) and interface charge density under the base electrode (right).

Atlas uses specific physical models and material parameters to take into account the mole fraction and doping of the AlGaN/GaN system [3]. We chose to model low field mobility using the ALBRCT model allowing the separate control of electrons and holes. We selected a nitride-specific high field mobility model by specifying GANSAT.N on the MODEL statement. In order to take into account the relatively deep ionization levels for acceptors in p-type GaN, we set the INCOMPLETE parameter on the MODEL statement [4]. In the simulation of high current operation, self heating effect may be important. We set the LAT.TEMP parameter on the MODEL statement to enable the heat flow simulation by the GIGA module. As for the breakdown simulation, an impact ionization model should be taken into account. We can use the tabular Selberherr model with the build-in parameters for GaN.

Performance of GaN device and convergence of its simulation can be significantly influenced by the presence of defects. We introduced bulk and interface traps by setting DOPING and INTTRAP statements in this Super HFET simulation. Threshold voltage and substrate leakage current are controlled by a concentration of acceptor and donor traps in the GaN buffer layer, respectively. Moreover, we put the interface traps to represent Fermi level pinning at the bottom of the GaN buffer. This assumption is properly valid because an actual GaN epitaxial layer has quite many defects around the interface with the substrate. It should be noticed that these traps play an important role in the convergence of the device simulation including a floating undoped-GaN buffer region.

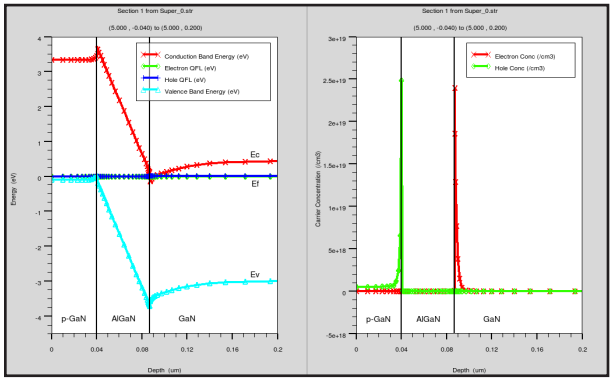

Figure 2. Band diagram (left) and vertical carrier profile (right) under the base electrode.

Simulation Results and Discussions

Figure 2 shows the band diagram and the vertical carrier profile under base electrode calculated at zero bias condition. As reported in [2], the accumulation of 2DEG and 2DHG has been verified at the lower and upper heterointerfaces, respectively.

The simulation results of the Id-Vg and Id-Vd characteristics are shown in Figure 3 and Figure 4, respectively. Very good agreement between simulations and experiments were obtained by setting some parameters properly. For example, the donor trap density in the GaN buffer determines the substrate leakage current and the acceptor trap density in GaN buffer affects the threshold voltage and the maximum drain current. The ALPHA parameter on the THERMCONTACT statement has an impact on the negative differential resistance at high current operation as well as the maximum drain current.

Figure 5 shows the breakdown characteristics and the impact generation rate distribution calculated by using slow transient simulation [3]. An increase of the gate current (including the base current) is observed near breakdown and the value is of the same order as the drain current. In addition, it should be noticed that impact ionization occurs near the drain-side edge of p-GaN region. These results indicate that breakdown voltage is dominated by the hole current into the base electrode through the p-GaN layer.

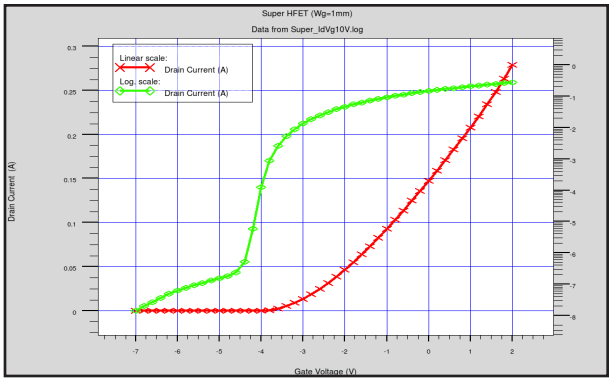

Figure 3. Simulated Id-Vg characteristics of the GaN Super HFET.

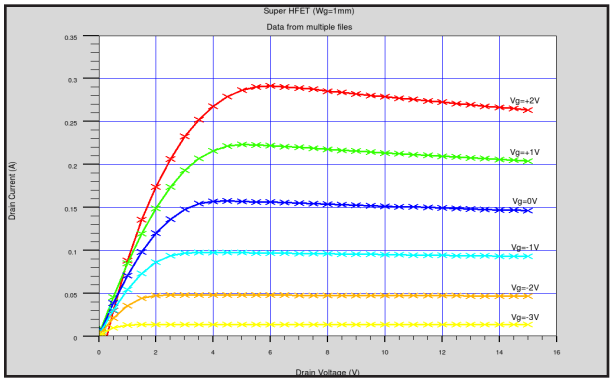

Figure 4. Simulated Id-Vd characteristics of the GaN Super HFET.

Conclusion

We have successfully demonstrated Atlas device simulation of a GaN-based Super HFET using the polarization junction concept. This device has many factors of convergence difficulty such as large polarization charges and abrupt heterojunctions as well as the existence of a p-GaN base region and a floating undoped-GaN buffer region. Owing to its sophisticated physical models, Atlas has proved to be capable of ensuring well-converged solutions with the device characteristics consistent with reference [1]. It allows users to speed up the product design process and shorten the development period.

References

[1] A. Nakajima, Y. Sumida, M. H. Dhyani, H. Kawai, and E. M. S. Narayanan, "GaN-based super heterojunction field effect transistors using the polarization junction concept," IEEE Electron Device Lett., vol. 32, no. 4, p.p. 542-544, Apr. 2011.

[2] A. Nakajima, Y. Sumida, M. H. Dhyani, H. Kawai, and E. M. S. Narayanan, "High density 2-D hole gas induced by negative polarization at GaN/AlGaN heterointerface," Appl. Phys. Express, vol. 3, no. 12, p. 121004, Dec. 2010.

[3] "State of the art 2D and 3D process and device simulation of GaN-based devices," Simulation Standard, July, August, September 2013.

[4] *Atlas User's Manual.*

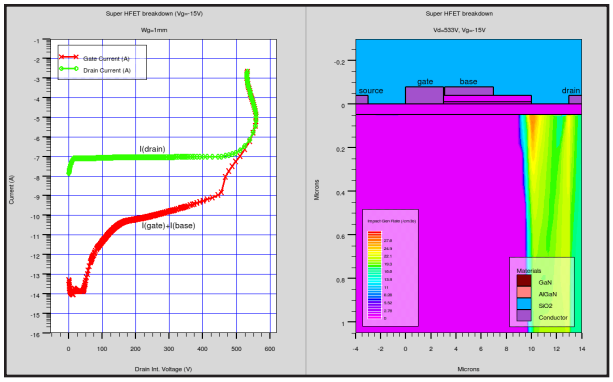

Figure 5. Breakdown characteristics (left) and impact generation rate distribution in the GaN Super HFET (right).

Hints, Tips and Solutions

Q: In Victory Device, how do I illuminate my 3D device in an opto-electronic simulation?

A: The 2 basic commands needed to illuminate a structure in Victory Device are *BEAM* and *SOLVE*. A single (or multiple) *BEAM* statement(s) are specified containing the light source properties. The *SOLVE* statement is used to execute a BEAM at a user-defined optical intensity.

Top-Down Blanket Illumination

To perform a top-down blanket illumination, an example *BEAM* statement would be:

BEAM NUM=1 X.ORIGIN=2 Y.ORIGIN=2 Z.ORIGIN=-5 PHI=0 THETA 90 WAVELENGTH=0.5 SAVE.RAYS

Which specifies that beam #1 is a illumination of wavelength= 0.5 μm that originates at xyz = (2, 2, -5) and approaches the structure from the top at an angle of 90° to the xy plane. The *SAVE.RAYS* option will save the rays to any subsequent saved structure. A *SOLVE* statement is then specified.

SOLVE B1=1

Solves the structure, with beam #1 applied at an optical intensity equal to 1 W/cm^2. The resulting structure is shown in Figure 1.

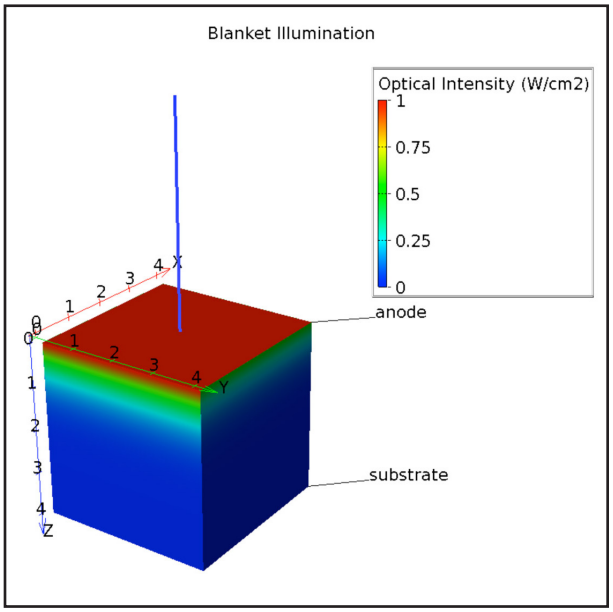

Figure 1. Top-down blanket illumination of a 3D block. The ray trace illustrates a beam origin of (2,2,-5). The contour plot illustrates an optical intensity of 1 W/cm^2 at the top surface.

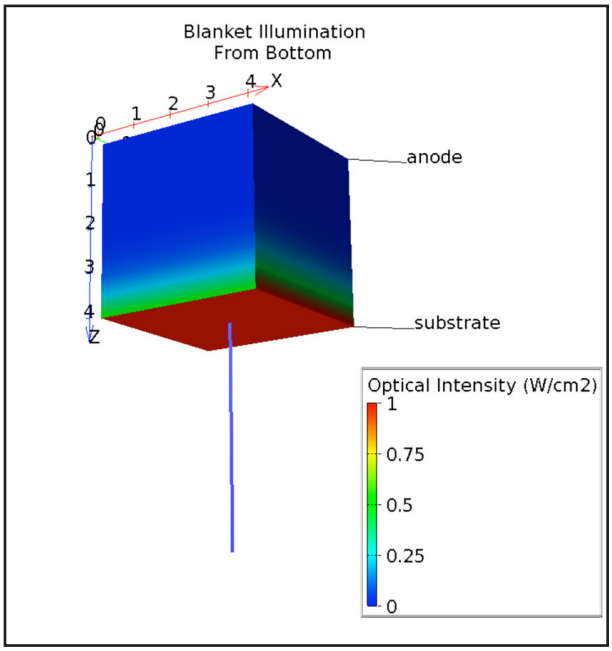

Figure 2. Bottom-up blanket illumination of a 3D block. The ray illustrates a beam origin of (2,2,9). The contour plot illustrates an optical intensity of 1 W/cm2 at the bottom surface.

Bottom-up Blanket Illumination

Alternatively, if a bottom-up blanket illumination is needed, the *BEAM* statement would be

BEAM NUM=1 X.ORIGIN=2 Y.ORIGIN 2 Z.ORIGIN=9 PHI=0 THETA=270 WAVELENGTH=0.5 SAVE.RAYS

The beam origin is now below the structure at xyz = (2,2,9), and approaches the structure from the bottom at an angle of 270° to the xy plane, as shown in Figure 2.

Beam Collimation Through a Window

Users may also want to collimate the light source through a defined window. This can be accomplished by including min/max values to the *BEAM* statement. Note, if min/max is not specified, the entire structure will be illuminated. A *BEAM* statement of

BEAM NUM=1 X.ORIGIN=2 Y.ORIGIN=2 Z.ORIGIN=-5 PHI=0 THETA=90 WAVELENGTH=0.5 SAVE.RAYS XMIN=-1 XMAX=1 ZMIN=-0.5 ZMAX=0.5

will crop (collimate) the beam, centered at x=2, y=2, through a is 2 μm by 1 μm window, as shown in Figure 3.

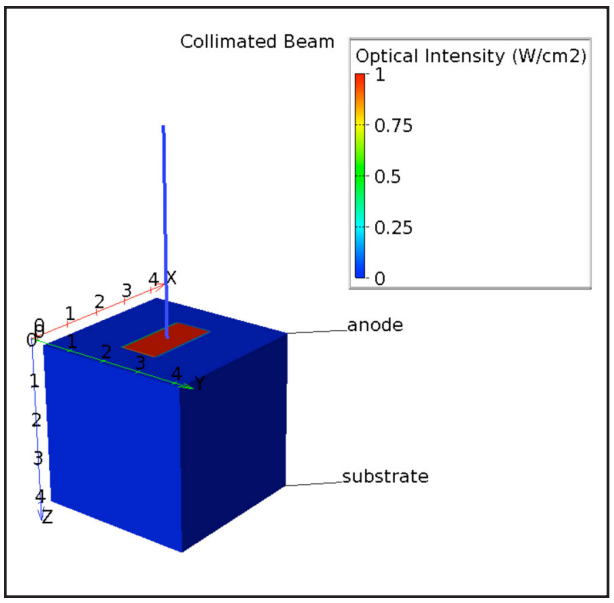

Figure. 3 1 Top-down collimated illumination of a 3D block. Optical intensity at the surface illustrates that the beam window is 2 µm by 1 µm.

Displaying Multiple Rays

As previously shown, displaying rays via Ray Trace in TonyPlot 3D is a useful illustrative tool to show the beam. It can also be helpful to increase the number of rays illustrated in a structure. This is set via the *NX* and *NZ* options in the *BEAM* statement. Setting *NX* and *NZ* both equal to 3 results in a 3x3 array of beams displayed, as shown in Figure 4.

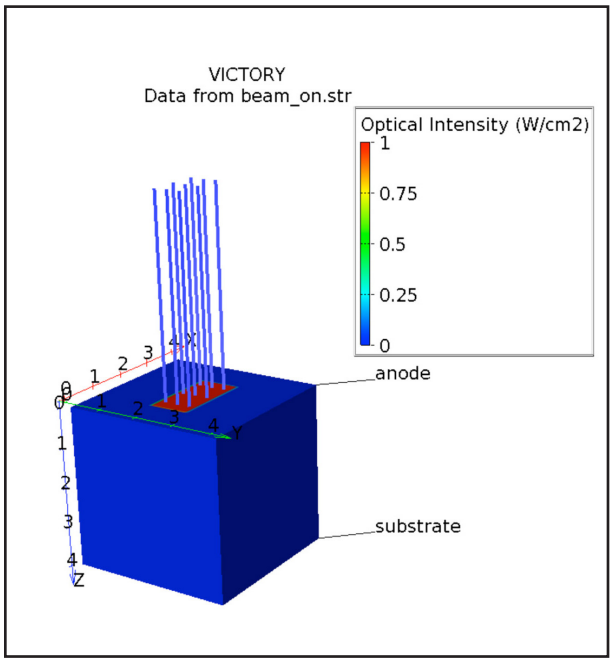

Figure 4. Setting nx=3 and ny=3 in the *BEAM* statement results in 9 rays to be illustrated in TonyPlot 3D.

Non-Normal BEAM Angles

Victory Device also allows simulation of beams at angles other than normal (90°) to the device surface. Modifying *BEAM* parameter *THETA* statement will change the angle of approach, relative to the xy plane, as seen in Figure 5.

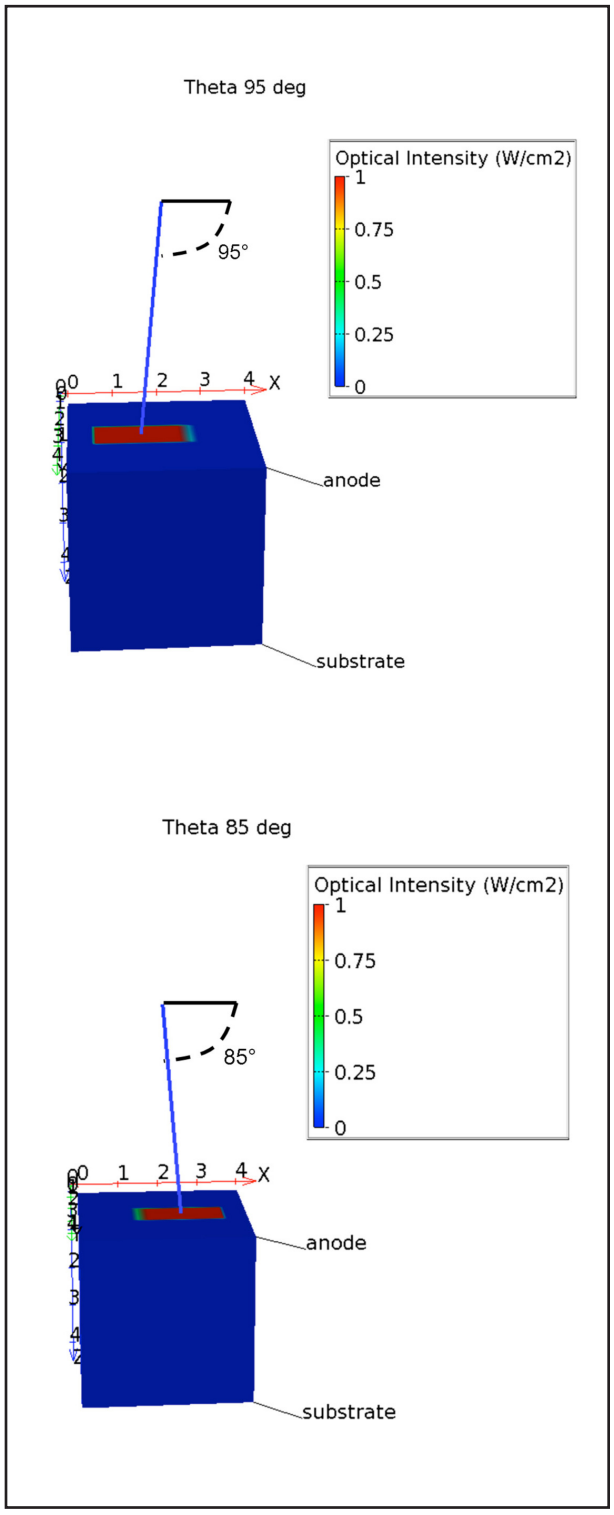

Figure 5. Examples of THETA = 95° (top) and 85° (bottom) to set the angle relative to the xy plane. Angle realative to the x-axis can also be set via *BEAM* parameter PHI.

Important Notes Regarding Angle and Origin

To get correct simulation results, it is required that the *BEAM* origin be defined as a point outside your 3D structure. Defining an origin within the structure is likely to produce incorrect results. Additionally, careful thought must be taken when defining *BEAM* parameters for origin (*X.ORIGIN*, *Y.ORIGIN* and *Z.ORIGIN*) and angles (phi and theta). If *BEAM* parameters are incorrectly defined, it can result in rays that are do not illuminate the 3D structure. By reviewing ray traces in the structure file via TonyPlot 3D, users can correctly define their *BEAM* statement.

Ray Splitting

If a user-defined *BEAM* is going to intersect more than one material regions, the ray will automatically be split. This allows efficient calculation of ray interaction in materials with differing refractive indices. Figure 6 illustrates how a single ray is split into two rays, the first intersecting silicon and the second intersecting the aluminum.

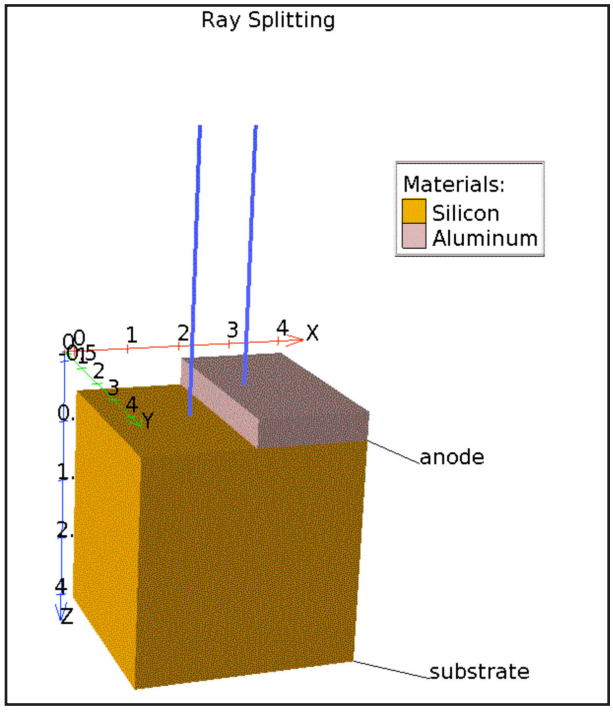

Figure 6. A single ray is split in two when intersecting different material regions, such as Silicon and Aluminum.

Reflections at Material Interfaces

By default, no reflected rays are traced. However, users may want to account for ray reflection of the front, sides or bottom of the 3D structure. For example:

BEAM NUM=1 X.ORIGIN=4 Y.ORIGIN=2 Z.ORIGIN=-5 PHI=0 THETA=100 WAVELENGTH=0.5 SAVE.RAYS XMIN=-0.5 XMAX=0.5 ZMIN=-0.5 ZMAX=0.5 REFLECTS=2 BACK.REFLECT

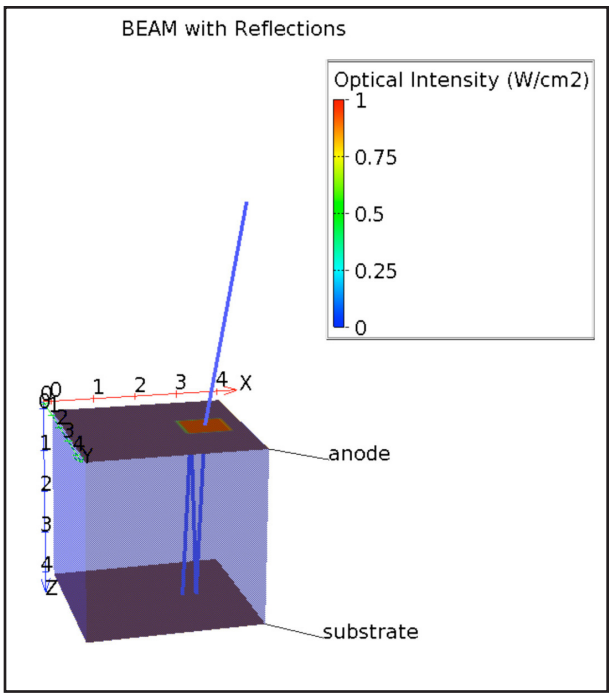

Figure 7. Illustration of ray reflection at the back of structure. The 3D silicon block is made transparent in TonyPlot 3D for visibility of rays.

will consider 2 reflections. In this case, only reflections with the back of the structure will be considered, as the back.reflect flag is active. Front reflections and sidewall reflections can also be included, as outlined in the Victory Device manual. Figure 7 illustrates the reflections off of the back surface.

Multi-Beam Illumination

Simulation is not limited to a single beam, as multiple beams can be defined. Each beam is defined with a *BEAM* statement with unique properties.

BEAM NUM=1 X.ORIGIN=4 Y.ORIGIN=2 Z.ORIGIN=-5 PHI=0 THETA=100 WAVELENGTH=0.5 SAVE.RAYS XMIN=-0.5 XMAX=0.5 ZMIN=-0.5 ZMAX=0.5

BEAM NUM=2 X.ORIGIN=0 Y.ORIGIN=2 Z.ORIGIN=-5 PHI=0 THETA=80 WAVELENGTH=0.5 SAVE.RAYS XMIN=-0.5 XMAX=0.5 ZMIN=-0.5 ZMAX=0.5

Again a *SOLVE* statement is specified to solve both beam numbers 1 and 2 concurrently, with intensities of 1 W/cm^2 and 2 W/cm^2 respectively:

SOLVE B1=1 B2=2

Figure 8 illustrates both beams intersecting the structure surface.

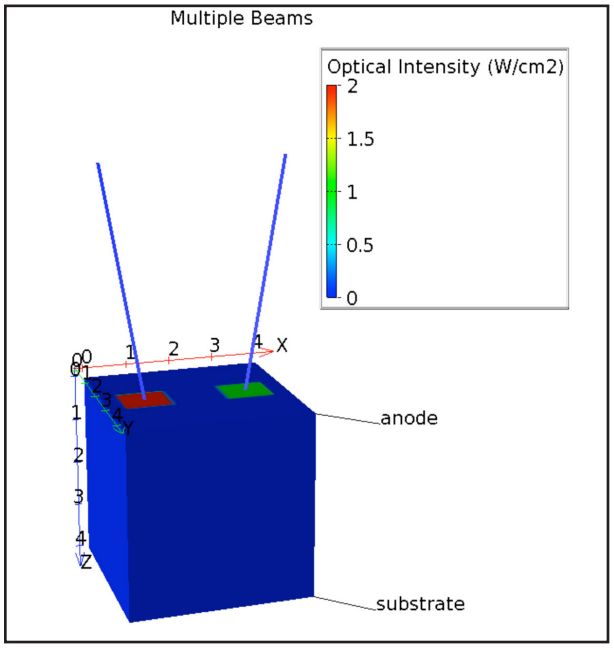

Figure 8. Two beams of different intensities (1 W/cm² and 2 W/cm²) the structure surface.

Optoelectronic Simulation Modes

A number of different optoelectronic simulation modes are available via the *SOLVE* statement.

1. Discrete Solve

SOLVE VGATE=1.2 B1=0.5 B2=1

The device structure will be solved at a static gate bias of 1.2 V, with two beams illuminating the device of intensities of 0.5 W/cm² and 1 W/cm².

2. Intensity Sweep

SOLVE B1=0.1 LIT.STEP=0.1 NSTEP= 4

The device structure will be solved, with the beam intensity stepped from 0.1 W/cm² to 0.5 W/cm² in 4 steps.

SOLVE B1=1E-7 LIT.STEP=10 NSTEP= 7 LMULT

Adding the lmult option will make the lit.step a multiplier, enabling a logarithmic sweep where the intensity is swept from 1e-7 W/cm² to 1 W/cm² in 7 steps.

3. Wavelength Sweep

SOLVE BEAM=2 LAMDA1=0.6 WSTEP=0.05 WFINAL=1.1

This will sweep the beam #2 wavelength from 0.6 μm to 1.1 μm in 50 nm increments.

4. Transient Analysis

To perform a transient optoelectronic simulation, users should first perform a steady state simulation.

SOLVE B1=1 B2=0.5 VGATE=1.2

Then the transient simulation can be initiated. In this case a 1 μs simulation. It is evident that beam #1 has been switched off and beam #2 intensity is increased.

SOLVE B1=0 B2=1 TSTEP=1E-11 TSTOP=1E-6

This instantaneous change in intensity is a bit unrealistic. Users can also specify a ramp time for the change in intensity.

SOLVE B1=2 B2=1.5 RAMP.LIT RAMPTIME=1E-9 TSTEP=1E-11 TSTOP=1E-7

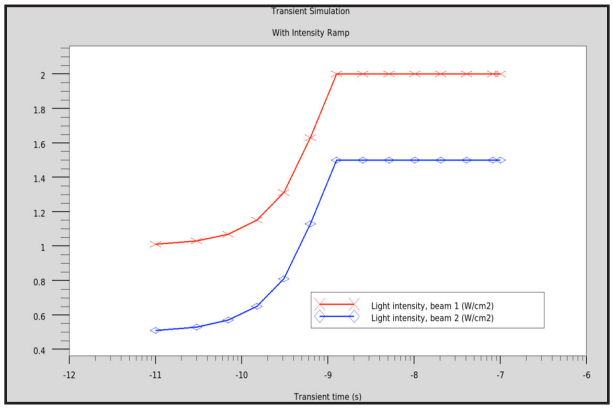

Figure 9. Beams #1 and #2 light intensities vs. time (on a lin-log scale). Light intensity is ramped over a 1 ns ramp time. Beam #1 intensity is increased from 1 W/cm² to 2 W/cm², and Beam #2 intensity is increased from 0.5 W/cm2 to 1.5 W/cm².

Additional Information

For additional information, including:

- User-defined photogeneration models
- Setting material optical properties
- Defining multi-spectral beams

as well as in-depth information on the topics presented here, please consult the Victory Device and TonyPlot 3D manuals or your contact local Silvaco support office.

Call for Questions

If you have hints, tips, solutions or questions to contribute, please contact our Applications and Support Department

Phone: +1 (408) 567-1000 Fax: +1 (408) 496-6080

e-mail: support@silvaco.com

Hints, Tips and Solutions Archive

Check out our Web Page to see more details of this example plus an archive of previous Hints, Tips, and Solutions

www.silvaco.com

Hints, Tips and Solutions

Q: How do I run a simulation on a cluster of computers using the distributed computing feature?

A new feature that is introduced in Silvaco's TCAD applications allows the user to run a parallel simulation on a cluster of computers within a network.

Currently this feature is supported in the solution of linear systems using the PAM solver. The PAM solver is a domain decomposition type solver which is parallelized with MPI – message passing interface.

There are many advantages to using distributed computing especially for large computationally intensive simulations:

- Splitting a large problem into smaller ones and computing them in parallel is clearly a superior approach with regards to performance. Simulation time can decrease by orders of magnitude.
- More resources are available to the simulation - the user is not limited by the number of CPUs or the total amount of memory on a specific computer.
- This approach provides a way of using the resources within the network efficiently.
- For certain very large problems it might be the only feasible approach, especially in cases when the amount of memory required exceeds the limits of any one available computer. As problem size increases this becomes more and more relevant.

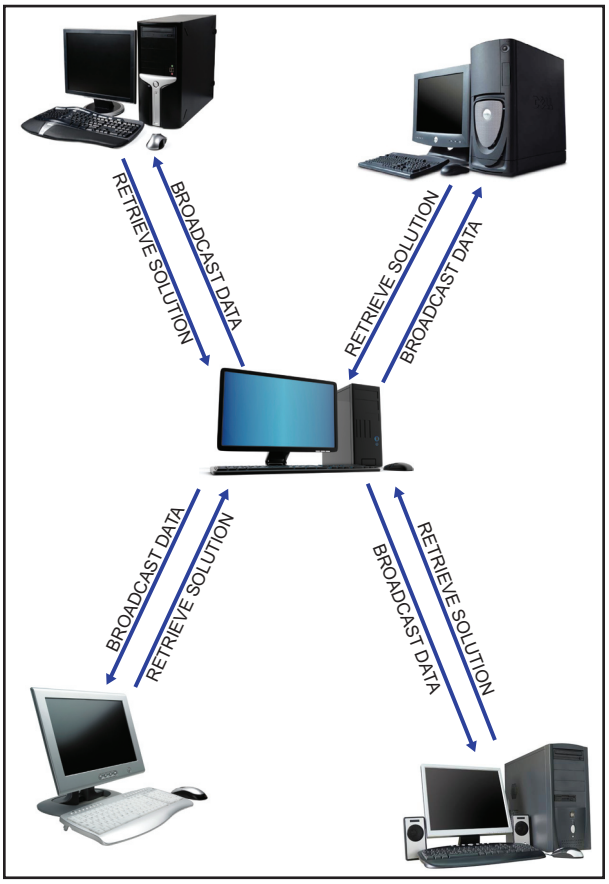

Figure 1.

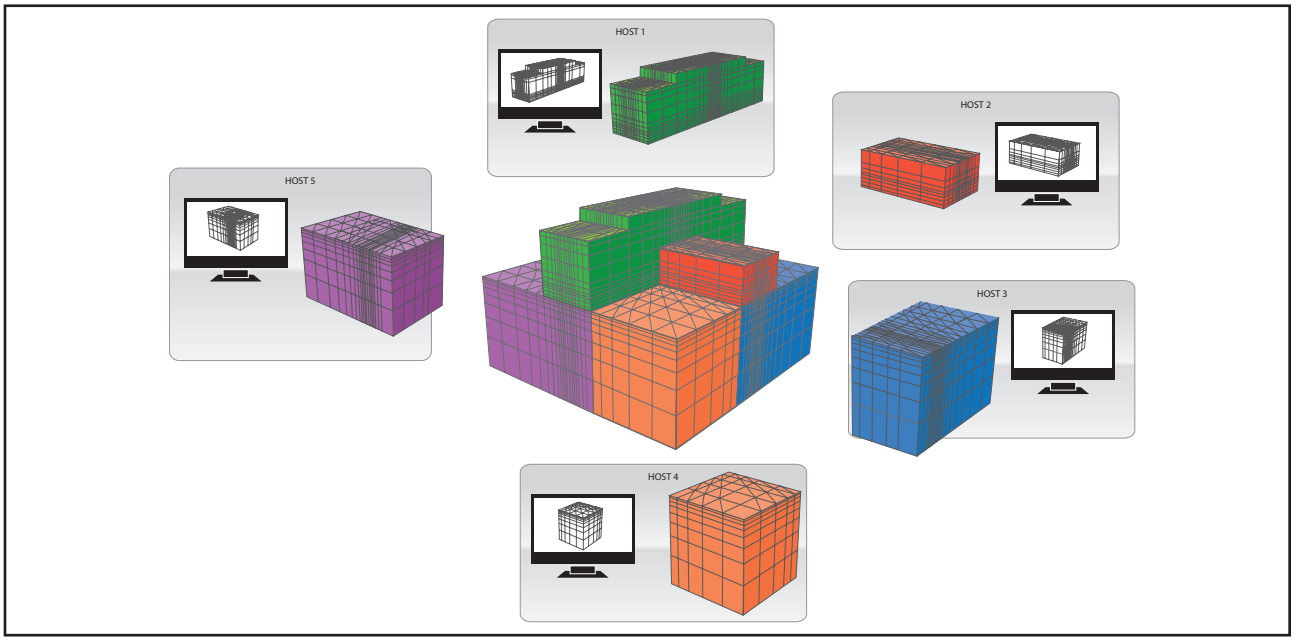

Figure 2.

To set up the distributed computing feature for the Silvaco TCAD applications on Linux:

1. List the names of the computers that will be used in a file. You can use the Linux command hostname to get the name. The name of the computer from which the simulation will be started should be placed first in the file.

   Example:
   The hostfile is named my-hosts and looks like this

   host1.Example.COM
   host2.Example.COM
   host3.Example.COM
   host4.Example.COM

The simulation will be running on the 4 machines listed above and will be started from host1.Example.COM

2. Set the environment variable SILVACO_MPI_HOSTS to the full path name of the hostfile my-hosts.

3. In order to be able to connect to remote hosts without being asked for a password for every simulation use RSA authentication. Run:

   shell$ ssh-keygen –t rsa

   Accept the default value for the file in which to store the key

   $HOME/.ssh/id_rsa and enter a passphrase.

   If you prefer not to use a passphrase you can skip that part.

   You can refer to the ssh documentation for more detailed information.

   Next copy a file generated by ssh-keygen:
   shell$ cd $HOME/.ssh
   shell$ cp id_rsa.pub authorized_keys

   In order for RSA authentication to work you need to have the $HOME/.ssh directory on all computers specified in the hostfile my-hosts. This might be already taken care of if your home directory is on a common filesystem. If not copy the $HOME/.ssh directory to your home directory on all computers in the hostfile.

   There will be four files in the $HOME/.ssh directory with the following permissions:

   -rw-r--r-- authorized_keys
   -rw------- id_rsa
   -rw-r--r-- id_rsa.pub
   -rw-r--r-- known_hosts

   Next ssh to each of the computers in the hostfile.

You will be asked for a password or a passphrase if you specified one above. If you have an ssh-agent program running the next time you try to ssh to the same computer the authentication will be done authomatically. You probably have ssh-agent running already.

Refer to ssh-agent documentation for further information how to launch ssh-agent in case you don't have one running.

You will also need to have a $HOME/.rhosts file on all computers listed in the hostfile. The $HOME/.rhosts file should contain the names of the computers and your user name.

Example:

For a user with user name tcaduser the $HOME/.rhosts should look like this:

host1.Example.COM tcaduser
host2.Example.COM tcaduser
host3.Example.COM tcaduser
host4.Example.COM tcaduser

Call for Questions
If you have hints, tips, solutions or questions to contribute, please contact our Applications and Support Department
Phone: +1 (408) 567-1000 Fax: +1 (408) 496-6080
e-mail: support@silvaco.com

Hints, Tips and Solutions Archive
Check out our Web Page to see more details of this example plus an archive of previous Hints, Tips, and Solutions

www.silvaco.com

USA Headquarters:

Silvaco, Inc.
4701 Patrick Henry Drive, Bldg. 2
Santa Clara, CA 95054 USA

Phone: 408-567-1000
Fax: 408-496-6080

sales@silvaco.com
www.silvaco.com

Worldwide Offices:

Silvaco Japan
jpsales@silvaco.com

Silvaco Korea
krsales@silvaco.com

Silvaco Taiwan
twsales@silvaco.com

Silvaco Singapore
sgsales@silvaco.com

Silvaco Europe
eusales@silvaco.com

SILVACO